

Hybrid Cobalt and Iron Based Metal Organic Framework Composites as Efficient Bifunctional Electrocatalysts towards Long-Lasting Flexible Zinc-Air Batteries

Weixin Li,^[a] Chen Wu,^[b, c] Hao Ren,^[b] Wei Fang,^[b] Lei Zhao,^[a] and Khang Ngoc Dinh^{*[b]}

Highly efficient and stable oxygen evolution reaction (OER) and oxygen reduction reaction (ORR) bifunctional electrocatalysts are urgently needed to realize the implementation of flexible rechargeable Zn-air batteries (ZABs). Herein, a series of hybrid Co and Fe based metal-organic frameworks (HCF-MOFs) are rationally designed and synthesized. The HCF-MOFs are directly used as electrocatalysts to enable oxygen catalysis. The unique hierarchical structure provides porous channels and ensures high exposure of metal sites, thus boosting the electrocatalytic activity. By composition regulation, the coordination environment of the active centers can be effectively modulated to achieve superior bifunctional oxygen electrocatalytic performance.

Specifically, an OER overpotential of only 295 mV at 10 mA cm^{-2} and an ORR half-wave potential of 0.82 V are obtained by the activated HCF-MOF, outperforming those of commercial RuO₂ and Pt/C. The results elucidate that HCF-MOF/OOH is formed during oxygen evolution, and serves as the active center. When combined with polyacrylate hydrogel electrolyte, the quasi-solid-state flexible ZAB based on HCF-MOF-3 delivers the maximum power density of 113.5 mW cm^{-2} , surpassing the Pt/C–RuO₂ counterpart. Significantly, the battery exhibits excellent durability whilst being subjected to bending tests. This work demonstrates the prospect of these HCF-MOFs as bifunctional electrocatalysts for high-performance ZABs.

1. Introduction

The ever-rising demand for clean energy storage has driven the accelerated development of non-flammable and high energy density rechargeable batteries. Among all candidates, Zn-air batteries (ZABs) have triggered lots of interest, especially for flexible electronics, due to the high-abundance of Zn, environmental friendliness, and remarkable theoretical energy density.^[1–3] Currently, the rechargeable ZABs suffer from poor energy efficiency and unsatisfied cycling durability, which is due to slow kinetics of the oxygen reduction reaction (ORR) and oxygen evolution reaction (OER) at air cathodes.^[4–6] In this regards, the best-performing electrocatalysts so far still rely on noble group metals (Pt, Ru, Ir and their alloys).^[7–9] Unfortunately, their high cost, reserve scarcity, and limited durability hinder their commercial applications.^[10] For the past 20 years, earth-abundant transition metal based catalysts, their hybrids or alloys with integration of various forms of conductive carbon (e.g. graphene, graphite, carbon black) have surged as promising bifunctional oxygen electrocatalysts.^[11–14] Common

ways of fabricating those efficient bifunctional electrocatalysts have been always combining with conductive substrates, ensuring large specific surface areas and abundant active sites.^[15,16] Various strategies have been adopted with great progresses; yet, the poor intrinsic catalytic activity and inherent degradation of catalysts largely impede their catalytic activity.^[17] Therefore, exploring active and robust bifunctional catalysts for high-performance rechargeable flexible ZABs is highly desired.

Metal-organic frameworks (MOF) assembled by metal ions and organic linkers are considered as one of the most promising family of electrocatalysts due to their structural diversity, tunable porosity, and adjustable chemical properties.^[18,19] Many types of MOF-derived nanomaterials, namely, oxides, phosphides, and functional carbon have been extensively investigated for electrocatalysis by virtue of their rich active sites, high electronic conductivity and homogeneous elemental doping.^[20–24] However, MOF-derived materials usually require high temperature pyrolysis and subsequent post treatments, which do not only hinder their large scale implementation but also result in inadequate control over particle size and distribution.^[25] From this perspective, using pristine MOF could simplify the fabrication process to a large extent while eliminate the concern regarding poor controlled pyrolysis. Despite those advantages, the inferior electrical conductivity and unsatisfied catalytic activities of MOF remain the major bottlenecks for their applications in electrocatalytic related areas.^[26]

Benefiting from the adjustable composition and structure of MOF, catalytic active sites could be finely tuned by either integrating hetero-atoms/ligands or constructing unsaturated coordination environment.^[27–29] Besides, modifying MOFs by

[a] Dr. W. Li, Dr. L. Zhao
The State Key Laboratory of Refractories and Metallurgy, School of Materials and Metallurgy, Wuhan University of Science and Technology, Wuhan 430081, China

[b] Dr. C. Wu, Dr. H. Ren, Dr. W. Fang, Dr. K. N. Dinh
School of Materials Science and Engineering, Nanyang Technological University, Singapore 639798, Singapore
E-mail: dinhngoc001@e.ntu.edu.sg

[c] Dr. C. Wu
State Key Laboratory of Power Metallurgy, Central South University, Changsha 410083, China

 Supporting information for this article is available on the WWW under <https://doi.org/10.1002/batt.202000163>

other conductive components, such as three-dimensional substrates (Ni foam),^[30] graphene oxide,^[26] and MXenes^[31] are also employed; thus, accelerating the charge and ion transfer processes. Although many strategies have been developed to modify MOF, adopting pristine MOF in rechargeable ZABs have been rarely studied and the relationship of oxygen electrochemical behaviors to the structure and composition of the MOF is still ambiguous. Therefore, it is imperative to design and discover the activity of MOF with the optimal conductivity, mass transfer, and active site density.

Herein, we report a series of hybrid pristine Co–MOF (PCO-MOF) @ pristine Fe–MOF (PFE-MOF) denoted as HCF-MOF by adjusting the molar ratio of Co/Fe ions for OER/ORR bifunctional electrocatalysis in flexible rechargeable ZABs. The as-synthesized HCF-MOF in the form of microspheres assembled by nanosheets is coated by numerous nanoparticles, which endows efficient channels for electrolytes and ions transport. Besides, using Co and Fe simultaneously could anticipate the interaction between different phases of metals; hence, efficiently enhancing OER and ORR activities. The activated HCF-MOF shows excellent electrocatalytic OER activities with a lower overpotential of 295 mV as compared to that of the commercial RuO₂ catalyst. It also performs well in ORR with onset potential and half-wave potential of 0.90 V and 0.82 V, respectively, along with limiting current density of 4.99 mA cm⁻². Furthermore, the assembled flexible ZAB based on HCF-MOF air-cathode with the sodium polyacrylate hydrogel as solid-state electrolyte shows a maximum power density of 113.5 mW cm⁻². The oxygen electrochemical mechanism in the HCF-MOF catalyst was also unraveled. Given the versatile structural and tunable chemical property of hybrid MOFs, this work offers an alternative strategy for rational design of efficient MOF-based composites for rechargeable ZABs.

2. Results and Discussion

In this work, HCF-MOFs were synthesized by co-assembly from mixtures of metals ions (Fe³⁺, Co²⁺) with 2-aminoterephthalic acid (BDC-NH₂) as the organic linker. By controlling the ratio of Co/Fe, a series of HCF-MOFs were obtained and denoted as

HCF-MOF-5, HCF-MOF-4, HCF-MOF-3, HCF-MOF-2. For comparison purposes, single metal MOF, namely PCO-MOF and PFE-MOF, were also prepared. XRD diffractograms of the PCO-MOF and HCF-MOF-3 show two prominent peaks at 8.7° and 17.6° corresponding to the (200) and (400) crystallographic planes of simulated Ni-based MOF (Figure 1a).^[32] In this structure, Co atom is in the center of the octahedral which is coordinated by six O atoms and further connected along the [010]/[001] direction in the (200) plane; thus, forming 2D structure separated by NH₂-BDC. However, no peaks of PFE-MOF can be detected in the HCF-MOF-3, which may be caused by the small contents of PFE-MOF in the hybrids. Notably, some Fe and Co atoms on the surface are coordinated with NH₂-BDC, resulting in coordinative unsaturated metal sites.^[33] After OER activation, additional diffraction peaks at around 11.6° and 23° are detected, indicating Co(Fe)OOH is formed during the electrochemical process (Figure S1). To further characterize the structure of the obtained MOFs, the FT-IR analyses of PFE-MOF, PCO-MOF, HCF-MOF-3, and OER-activated HCF-MOF-3 were conducted and shown in Figure 1b. The pronounced peak of NH₂-BDC at around 3300 cm⁻¹ can be attributed to the stretching vibrations of the N–H bond.^[34] Another two peaks at around 1690 cm⁻¹ and 1420 cm⁻¹ belong to the ν_s (–COO–) and ν_{as} (–COO–) in NH₂-BDC.^[35] In addition, these peaks in NH₂-BDC spectrum exhibit slight shift compared to those in PCO-MOF, PFE-MOF, and HCF-MOF-3 spectra, suggesting the successful coordination of metal ions with the linker molecules.^[36] Noteworthy, the peaks represented the interaction between metal atoms (Co and Fe) and the carboxylic groups (O=C=O) appeared at 511 cm⁻¹ and 565 cm⁻¹ in FT-IR spectra of PCO-MOF and PFE-MOF, respectively. These two peaks can also be detected in the HCF-MOF-3; hence, confirming that HCF-MOF-3 is a mixture of PCO-MOF and PFE-MOF. After OER activation, the ν_{as} (–COO–) and ν_s (–COO–) peaks become weak; whereas, the ν_s (–OH) peak at 3400 cm⁻¹ and water molecules peak at 1648 cm⁻¹ are prominent. It can be elucidated that CoO₆ or FeO₆ inside MOF were electro-oxidized into CoOOH or FeOOH which then play the role as active centers for OER.

Figure 2a–c show the SEM characterizations of PCO-MOF, PFE-MOF, and HCF-MOF-3, respectively. While PCO-MOF ap-

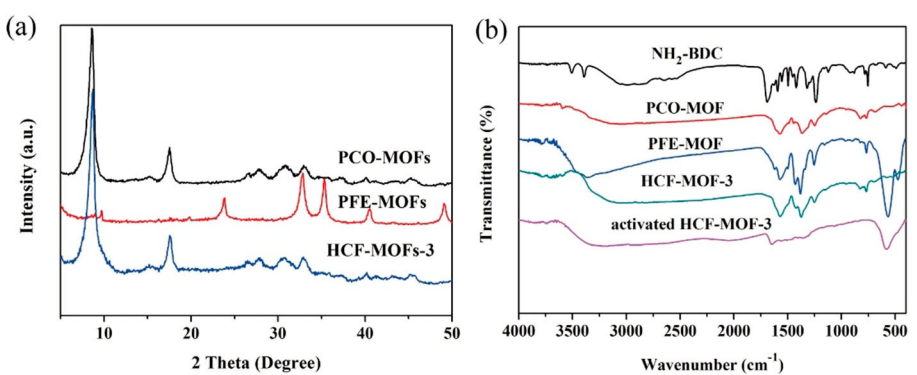


Figure 1. a) XRD diffractograms of PCO-MOF, PFE-MOF, HCF-MOF-3; b) FT-IR spectra of NH₂-BDC, PCO-MOF, PFE-MOF, HCF-MOF-3 and OER activated HCF-MOF-3.

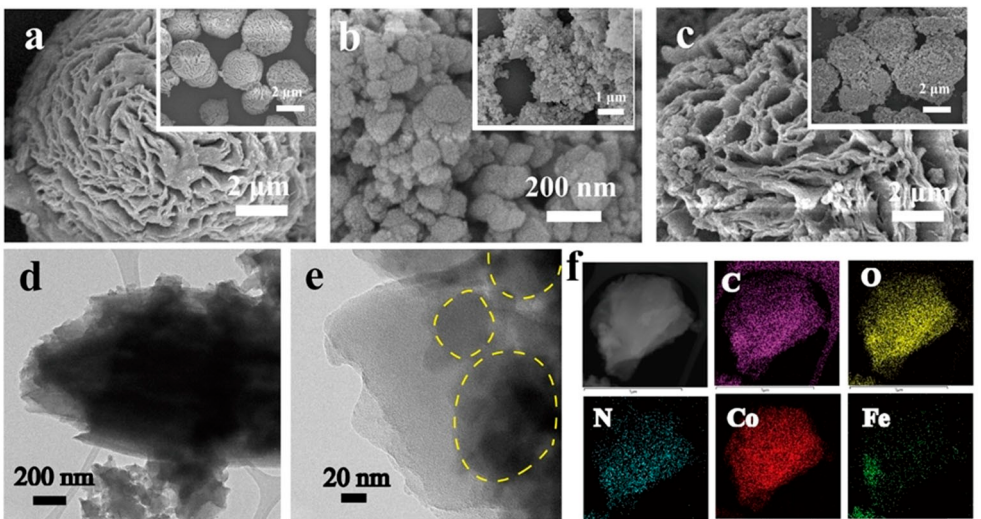


Figure 2. SEM images of a) PCO-MOF, b) PFE-MOF, and c) HCF-MOF-3; d) TEM and e) HRTEM images of HCF-MOF-3; f) EDX mapping images of HCF-MOF-3.

pears as microspheres assembled by 2D sheets, PFE-MOF exhibits as dispersive nanoparticles. Therefore, expectedly, the HCF-MOF-3 displays two distinct morphologies of 2D sheets assembled into microspheres and dispersive nanoparticles on the surface of microspheres (Figure 2c). As can be expected, layered MOFs could facilitate mass transport and electron transfer process. And these 2D sheets structure endow abundant accessible surface active sites thus promote the electrocatalytic process. These interconnected 2D sheets loaded with dispersive nanoparticles with porous channels can also effectively facilitate the contact of electrolytes with the catalysts owing to the high exposure of surface atoms. Besides, 2D MOF nanosheets possess higher electrical conductivity than its bulk counterpart due to the rich defects originated from the nanosheets structure.^[37,38] The vacancies in layered MOF can serve as shallow donors to increase the carrier concentration of $\text{Co}(\text{Fe})\text{O}_6$ units of the MOF, which is beneficial to the conductivity of MOF.^[39] Therefore, superior electrocatalytic performance could be obtained by directly using HCF-MOF-3 with the nanoparticles coated 2D sheets structure. The TEM characterization was also carried out to further explore its fine morphology and composition. Figure 2d–e reveal a 2D structure, certifying that the composites are assembled by nanosheets, and there are some particles on the surface of the nanosheets. High angle annular dark field (HAADF) image and scanning transmission electron microscopy energy-dispersive X-ray (STEM-EDX) elemental mapping in Figure 2f indicate the presence of Co, Fe, C, O, and N elements. The distribution of Fe mainly appears on the area of nanoparticles re-confirming that the nanoparticles are PFE-MOF, while the large 2D layer is PCO-MOF. The influence of Co/Fe ratio to the morphology of the obtained hybrids MOF is also investigated (Figure S2). The amount of nanoparticles on the surface of the microspheres increases as the Fe content increases. However, it is difficult to distinguish the substructure of nanosheets when the Co/Fe ratio is 2:1 due to the full coverage and aggregation of

nanoparticles which can hinder the exposed active metal sites. Therefore, appropriate hybridization of PCO-MOF and PFE-MOF may tune the exposed active sites to fully utilize the potential of the electrocatalyst. Furthermore, the morphology of the activated HCF-MOF-3 is shown in Figure S3 which indicates that the 2D layers are assembled by numerous nanosheets with round edges (Figure S3a). The HRTEM image of the OER-activated HCF-MOF-3 clearly exhibits lattice fringes of 0.231 nm and 0.208 nm, which are correlated correlating to the (012) plane of CoOOH and (120) plane of FeOOH , respectively (Figure S3d). The in-situ generation of $-\text{OOH}$ species during OER process can enhance OER activity. Besides, the element distribution of OER activated HCF-MOF-3 remains unchanged (Figure S3b).

Subsequently, the chemical composition and oxidation state of PCO-MOF, PFE-MOF, HCF-MOF-3, and OER activated HCF-MOF-3 were analyzed by XPS. The XPS survey spectrum demonstrates the presence of Fe, Co, O, C, and N in HCF-MOF-3 (Figure S4). The high-resolution Co 2p XPS spectrum of PCO-MOFs (Figure 3a) displays two main signals at 781.18 and 797.68 eV, which can be assigned to $\text{Co } 2\text{p}_{3/2}$ and $\text{Co } 2\text{p}_{1/2}$, respectively.^[35] Also, two shakeup satellite are seen at 786.58 and 802.78 eV. Compared to PCO-MOF, the electron binding energy of $\text{Co } 2\text{p}_{3/2}$ for HCF-MOF-3 shifts to lower binding energy by 0.2 eV. Figure 3b displays the Fe 2p XPS spectrum of HCF-MOF-3 with two main peaks at 724.28 and 711.68 eV, which are ascribed to $\text{Fe } 2\text{p}_{1/2}$ and $\text{Fe } 2\text{p}_{3/2}$, respectively.^[39] Besides, two satellites with binding energies of 732.18 and 718.98 eV are also observed, revealing the existence of Fe^{3+} .^[40] Noteworthy, the binding energy of $\text{Fe } 2\text{p}_{3/2}$ in PFE-MOF shifts to lower value of 710.98 eV. This kind of peak shift implies a strong electronic interactions between PCO-MOF and PFE-MOF, which is contributed by the inter-molecular synergistic effects. These XPS results indicate that the metal center ion in HCF-MOF-3 is modified, and the Co center possesses increased electron density; thus, accelerating the charge transfer process

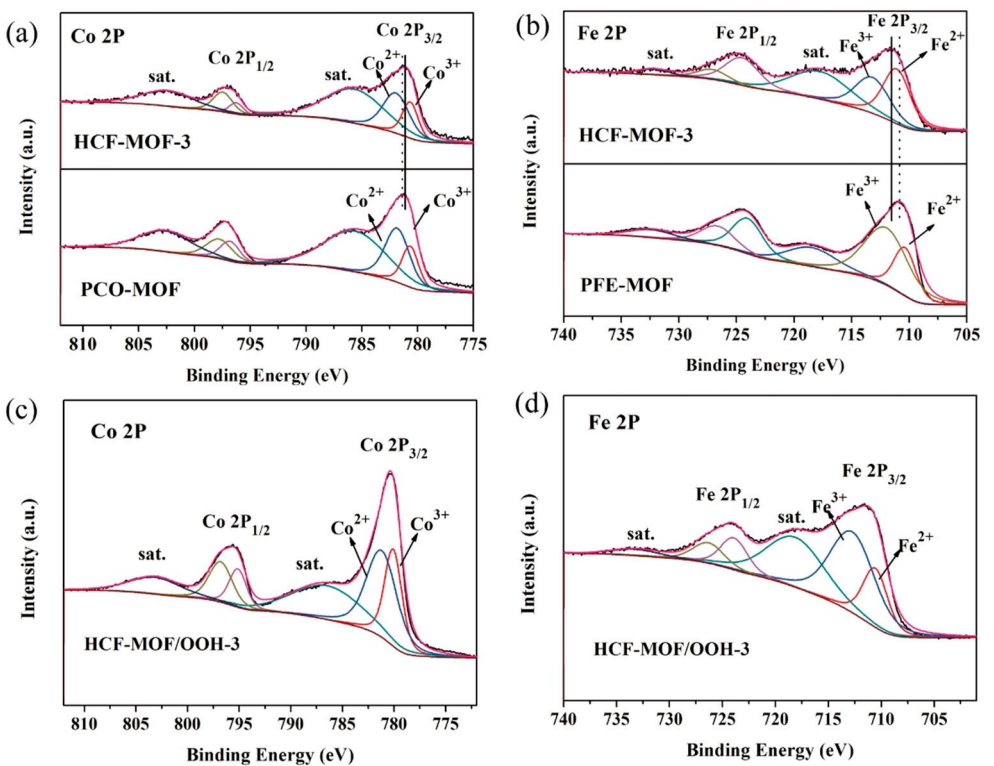


Figure 3. XPS spectra of a,c) Co 2p spectra and b,d) Fe 2p spectra.

and improving the OER catalytic activity.^[41,42] After the OER activation, both the ratio of Co³⁺/Co²⁺ and Fe³⁺/Fe²⁺ increase, suggesting the formation of oxyhydroxides (OOH) species, which are beneficial to OER performance (Table S1). Furthermore, the N 1s, O 1s, and C 1s XPS spectra of HCF-MOF-3 and HCF-MOF/OOH-3 are presented in Figure S4. The O 1s peaks can be deconvoluted into the O=C=O (531.70 eV), C–O (533.27 eV), and O–H (534.05 eV). The small shift of O 1s binding energy after OER activation accounting for lattice oxygen and OOH species can be observed as in Figure S4c. The C 1s and N 1s XPS spectra remains the same after OER activation, suggesting that the structure of MOF is kept. Both XPS and TEM results verify the formation of surface-oxidized Co (Fe)OOH after OER activation process; hence, implying HCF-MOF/OOH-3 is the active material in catalysis process. Moreover, the introduction of -NH₂ into MOF may enhance the catalytic activity of MOF by changing coordination environment of the metal centers.^[43]

Furthermore, Raman spectra are shown in Figure S5. Compared with HCF-MOF-3, the additional prominent peaks at 660 and 928 cm⁻¹ for HCF-MOF/OOH-3 are associated with OOH species.^[44,45] Combined with the XRD, TEM and XPS results, it can be speculated that the surface of HCF-MOF-3 was oxidized into Co(Fe)OOH after OER activation; thus, making HCF-MOF/OOH-3 the real active material in for OER electrocatalysis. Besides, the intensity ratio of D and G band (I_D/I_G) on HCF-MOF/OOH-3 is enhanced, suggesting the higher number of defects sites after activation, which is beneficial for catalytic applications.^[24]

To gain insight into catalytic properties of the synthesized catalysts, OER performance was investigated in the O₂-saturated 1.0 M KOH. The catalyst loading on the glassy-carbon supporting electrode is fixed at 0.4 mg cm⁻². Prior to OER performance measurement, 10 cycles of cyclic voltammetry (CV) scan is conducted to activate the original MOF. Figure 4a presents obtained polarization curves without Ohmic correction. It can be seen that the HCF-MOF/OOH-3 shows the lowest overpotential of 295 mV to deliver 10 mA cm⁻², outperforming the PCO-MOF/OOH (340 mV), PFE-MOF/OOH (421 mV) and the benchmark commercial RuO₂ (351 mV). Besides, the Tafel slope of HCF-MOF/OOH-3 (44 mV dec⁻¹) is smaller than those of PCO-MOF/OOH (59 mV dec⁻¹), PFE-MOF/OOH (58 mV dec⁻¹), and RuO₂ (89 mV dec⁻¹), suggesting favorable kinetics after hybridization (Figure 4b). It is worth to note that HCF-MOF/OOH-3 shows the optimal OER performance as compared to hybrids with other molar ratios (Figure S6). These results demonstrate that suitable incorporation of PFE-MOF/OOH could utilize the synergistic effect within the hybrid. Meanwhile inappropriate increased amount of PFE-MOF/OOH can lead to the blockage of the pores and Co sites in PCO-MOF/OOH, which is detrimental to the OER process. Figure S7a compares the first CV cycle of HCF-MOF-3 with the subsequent second and third cycles. A prominent anodic oxidative peak is observed in the first CV cycle, while the peak intensity reduces dramatically in the following cycle (2nd and 3rd cycle). It implies the surface oxidation of HCF-MOF-3 into Co(Fe)OOH; similar phenomenon has been reported previously for Co(OH)₂ and CoO_x.^[46] Note-worthy, the oxidative peak shifts to higher potential with the

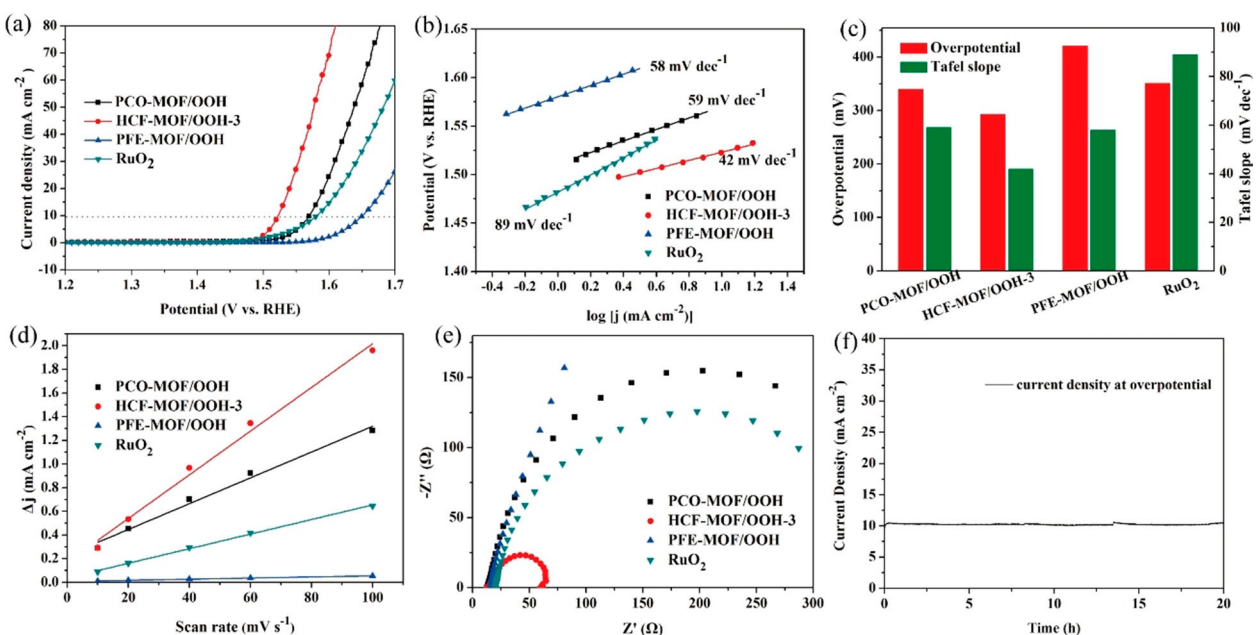


Figure 4. a) OER polarization curves of PCO-MOF/OOH, HCF-MOF/OOH-3, PFE-MOF/OOH, and RuO₂; b) their corresponding Tafel plots. c) Overpotential and Tafel slope values of the obtained catalysts. d) Dependence of the capacitive current vs scan rates. e) Electrochemical impedance spectra. f) Chronoamperometric response of HCF-MOF/OOH-3. Measurements were done in 1.0 M KOH solution.

decrease of the Co/Fe ratio (Figure S7b), indicating higher difficulty in oxidizing Co²⁺ at higher Fe content due to the strong electronic interaction between the Co and Fe.

In order to understand the difference in OER activities of these catalysts, the electrochemical surface areas (ECSA) were acquired by estimating the double-layer capacitances (C_{dl}) from the CV in the non-Faradaic region (Figure S8). As seen from Figure 4d, HCF-MOF/OOH-3 exhibits higher C_{dl} (18.46 mF cm⁻²) as compared to PCO-MOF/OOH (10.90 mF cm⁻²) and PFE-MOF/OOH (0.48 mF cm⁻²), demonstrating increased electrochemical active sites and effective electrode-electrolyte interface area. More importantly, the results of intrinsic activity of the obtained catalysts (Figure S9), which are evaluated by normalization of polarization curves by ECSA, deliver the same trend as that of ECSA.^[35,47] The HCF-MOF/OOH-3 exhibits the highest intrinsic catalytic activity by means of overpotential and Tafel slope. To gain deeper understanding of the catalytic kinetic of the electrodes, EIS measurements were conducted and the results are shown in Figure 4e. The charge transfer resistance (R_{ct}) of HCF-MOF/OOH-3 is significantly lower than those of PCO-MOF/OOH, PFE-MOF/OOH, and RuO₂. It indicates the fastest charge transfer at the HCF-MOF/OOH-3 and electrolyte interface during OER, which is consistent with the high activity shown above. This can be attributed to the interaction between different phases of metals and the formation of numerous nanosheets throughout 2D layers assembled microsphere after OER activation, which can facilitate mass transport and supply abundant exposed active metal ion centers for better utilization of the as-prepared catalyst. Moreover, the 2D layers structure composed by carbon-based linker can maintain the uniform distribution of active sites and avoid the agglomeration of active Co(Fe)OOH species. Equally important to catalytic

activity, Figure 4f illustrates the stability tests of the HCF-MOF/OOH-3, which exhibits excellent stability toward OER under chronoamperometry test for 20 h. Furthermore, XRD and SEM measurements were performed to investigate the stability of HCF-MOF/OOH-3 after durability experiment (Figure S10). As can be seen from XRD and SEM results, HCF-MOF/OOH-3 shows negligible change in term of crystal structure and morphology, thus implying the good stability of the material.

Towards ZABs application, the ORR electrocatalytic behaviors of the prepared catalysts were studied. 10 cycles of cyclic voltammetry (CV) scan is conducted to activate the original MOF before ORR performance measurement as well. Figure 5a shows the ORR polarization curves collected on RDE at a rotating speed of 1600 rpm. As can be seen, HCF-MOF-3 achieves a high onset-potential (E_{onset}) and an admirable half-wave potential ($E_{1/2}$) of 0.90 V and 0.82 V, respectively. These performance indicators are comparable to those of the benchmark Pt/C ($E_{onset} = 0.92$ V; $E_{1/2} = 0.83$ V), and surpass those of single-metal MOF including PCO-MOF ($E_{onset} = 0.86$; $E_{1/2} = 0.79$ V) and PFE-MOF ($E_{onset} = 0.85$ V; $E_{1/2} = 0.78$ V). Besides, the diffusion limiting current density (j_L) of HCF-MOF-3 at 1600 rpm is measured to be 4.99 mA cm⁻². Additionally, HCF-MOF-3 shows a modest Tafel slope of 37 mV dec⁻¹ (Figure 5b), even smaller than that of Pt/C (60 mV dec⁻¹), indicating a better kinetics during ORR process. Figure S11 gives the composition effect of HCF-MOF on the ORR catalytic activity, which also proves that HCF-MOF with Co to Fe molar ratio of 3 to 1 owns the best activity. Moreover, the electron transfer number (n) per O₂ reduced of HCF-MOF-3 was studies by linear sweep voltammetry at different rotation speeds based on K-L equation. The K-L plot at different potentials were derived (Figure 5d), from which

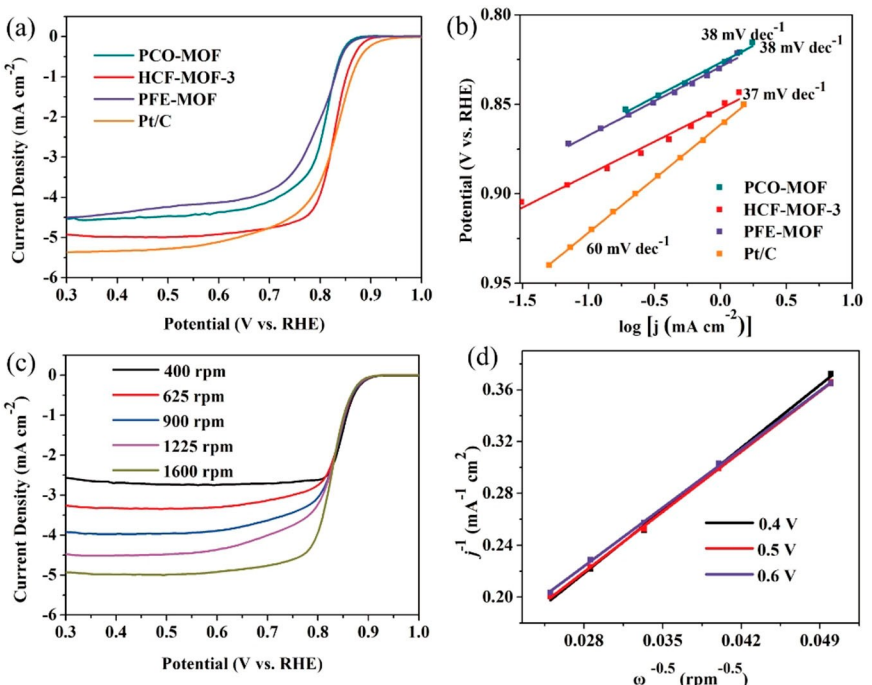


Figure 5. a) ORR polarization curves of catalysts measured at the electrolyte solution of 0.1 M KOH saturated with O₂ using RRDEs at 1600 rpm, b) Tafel plots, c) polarization curves of HCF-MOF-3 at various rotation rates, and d) the Koutecky-Levich plots.

n is found to be approximately 4, indicating that the ORR process is dominated by 4-electron pathway.^[48]

Apart from the catalytic activity, long-term durability of the catalyst was also investigated. The chronoamperometry response at 0.7 V (vs. RHE) is displayed in Figure S12a, in which a current retention of 98% is obtained after 20 hours. When subjected to methanol cross-over test, better resistance than that of Pt/C is also seen in Figure S12b, indicating its impressive resistance to corrosion and poisoning in alkaline solution.

The oxygen bifunctionality of electrocatalysts can be evaluated by the overpotential gap between ORR and OER ($\Delta E = E_{10} - E_{1/2}$). In this manner, HCF-MOF-3 performs the best at 0.705 V, surpassing those of Pt/C, RuO₂ with 0.95 V, 1.13 V, respectively, which signifies the outstanding catalytic reversibility of HCF-MOF-3 (Figure S13). Based on the above detailed discussions, it can be clarified that the OER and ORR performance of the activated HCF-MOF-3 are among one of the highest performances of reported excellent transition metal or carbon-based bifunctional catalysts (Table S2).

To this end, we have seen the potential of HCF-MOF-3 as air electrodes for ZABs through its outstanding OER-ORR bifunctional catalytic activity. Therefore, a rechargeable flexible solid ZAB made of HCF-MOF-3 air cathode was fabricated in which the alkaline polyacrylate hydrogel was employed as the quasi-solid state electrolyte. Reference batteries were also constructed using electrodes containing the mixture of commercial Pt/C–RuO₂. Firstly, the fabricated HCF-MOF-3 based ZAB indicates a decent open circuit voltage of 1.38 V (Figure 6a), which is marginally higher than that of the precious metals based ZABs (1.31 V). In Figure 6b, HCF-MOF-3 exhibits a slightly smaller charge-discharge voltage gap compared with the Pt/C–RuO₂ mixture in a broad range of current density (1–100 mA cm⁻²). However, noticeably, the HCF-MOF-3 based ZABs offers a high current density of 100 mA cm⁻² at 0.86 V discharge voltage, corresponding to incredibly-high power density of 113.5 mW cm⁻² (Figure 6c). These values are even rival the recently published aqueous ZABs (Table S3). Continuous discharging ZAB with HCF-MOF air electrode at 10 mA cm⁻² until dead results in a specific capacity of 524 mAh g⁻¹ and energy density of 618.3 Wh kg⁻¹. Meanwhile, Pt/C–RuO₂ ZAB show smaller numbers of 501 mAh g⁻¹ and 571.1 Wh kg⁻¹ in the same test (Figure 6d).

Additionally, the rechargeability of the ZAB based on HCF-MOF-3 was also investigated in comparison with that of noble metal counterpart. Figure 6e show the pulse charge-discharge cycling profiles at 2 mA cm⁻² (5 min discharge followed by 5 min charge, 10 min for each cycles). The HCF-MOF-3 air cathode shows an initial round trip efficiency of 62% (discharge voltage and charge voltage of 1.20 V and 1.93 V, respectively), slightly better than 58% of Pt/C–RuO₂ one. Noteworthy, while the benchmark noble metal air cathode shows a continuous decrease in energy efficiency to 50% after 50 cycles; the HCF-MOF-3 based ZAB presents excellent cycling performance for 400 cycles (no significant change in voltage gap). Therefore, the HCF-MOF-3 ZAB exhibits superior performance and stability over its counterpart based on Pt/C–RuO₂ air-cathode.

The outstanding ZABs performance of the HCF-MOF cathode catalyst is attributed to the unique hierarchical structure with nanosheets and nanoparticles sub-units, which endows efficient channels for electrolytes and ions transport and enables the fast diffusion of oxygen/hydroxyl. Also, the coordination environment is optimized by synergistic effect of

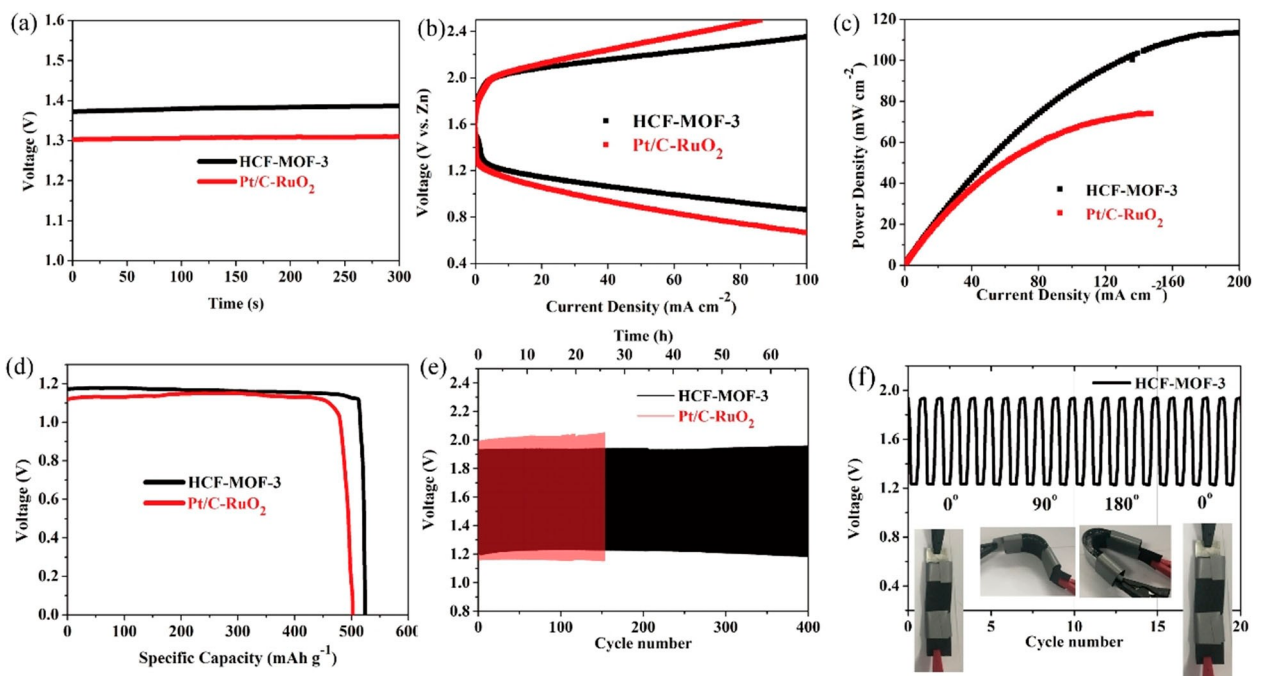


Figure 6. Performance of flexible solid-state ZABs based on HCF-MOF-3 and Pt/C-RuO₂ cathode catalysts: a) open-circuit voltages, b) charge-discharge curves, c) power density plots, d) discharge curves at 10 mA cm⁻², e) charge-discharge cycling curves of ZABs at 2 mA cm⁻², and f) cycling performance of the battery with the HCF-MOF-3 cathode at various bending angles.

PCO-MOF and PFE-MOF; thus, further facilitating the ORR and OER processes during discharge and charge, respectively.

To meet the requirement of application in portable and wearable devices, the performance of the solid state ZAB composed of HCF-MOF-3 air cathode was also tested under various deformation. As shown in Figure 6f, at different bending states of 0°, 90°, 180°, and back to 0°, the battery still capable of maintaining extremely stable discharge-charge plateaus, suggesting the excellent flexible prospect. As a proof-of-concept of its application for mobile devices, three solid state HCF-MOF-3 based ZABs were connected in series to charge an Android smartphone (Figure S14, and Supplementary video). As expected, the Android smartphone can be charging once connecting with HCF-MOF-3 based ZABs. These superb performance indicators along with the successful demonstration make HCF-MOF-3 one of the most promising cathode catalyst for rechargeable metal air battery technologies

3. Conclusions

In conclusion, a series of HCF-MOFs have been successfully fabricated with the unique hierarchical structure assembled by subunits of nanosheets and nanoparticles, thus providing porous channels for electron and mass transport. The electrocatalytic activity can be optimized by the modulation of coordination environment via the synergistic effect of PCO-MOF and PFE-MOF. Due to the formation of oxyhydroxides (OOH) species, HCF-MOF/OOH-3 acts as the active center and demonstrates the modest OER overpotential of 295 mV at

10 mA cm⁻² with a small Tafel slope of 42 mV dec⁻¹, outperforming the commercial RuO₂ catalysts by a considerable margin. Besides, the half-wave potential towards ORR of HCF-MOF-3 is as high as 0.82 V. As the air-cathode for quasi-solid state flexible ZAB, it could exhibit a decent open circuit voltage of 1.38 V and high power density of 113.5 mW cm⁻², which outperform those of the commercial Pt/C-RuO₂ catalyst. The flexible ZABs can work stably in long-time cycling and even under different bending conditions, which demonstrating a great potential application in portable wearable devices.

Supporting Information

Supporting Information is available from the Wiley Online Library or from the author.

Acknowledgements

This work was financially supported by the Natural Science Foundation of Hubei Provincial (2017CFB291), China Scholarship Council (201808420125). The authors thank the Facility for Analysis, Characterization, Testing and Simulation (FACTS) of Nanyang Technological University, Singapore, for technical support.

Conflict of Interest

The authors declare no conflict of interest.

Keywords: bifunctional catalysts • electrocatalysis • metal-organic frameworks • hierarchical structures • flexible zinc-air batteries

- [1] B.-Q. Li, S.-Y. Zhang, B. Wang, Z.-J. Xia, C. Tang, Q. Zhang, *Energy Environ. Sci.* **2018**, *11*, 1723–1729.
- [2] Y. Guo, P. Yuan, J. Zhang, Y. Hu, I. S. Amiiniu, X. Wang, J. Zhou, H. Xia, Z. Song, Q. Xu, S. Mu, *ACS Nano* **2018**, *12*, 894–1901.
- [3] K. N. Dinh, Z. Pei, Z. Yuan, V. C. Hoang, L. Wei, Q. Huang, X. Liao, C. Liu, Y. Chen, Q. Yan, *J. Mater. Chem. A* **2020**, *8*, 7297–7308.
- [4] J. Wang, X. Zheng, Y. Cao, L. Li, C. Zhong, Y. Deng, X. Han, W. Hu, *ACS Appl. Mater. Interfaces* **2020**, *12*, 8115–8123.
- [5] S. Liu, M. Wang, X. Sun, N. Xu, J. Liu, Y. Wang, T. Qian, C. Yan, *Adv. Mater.* **2018**, *30*, 1704898.
- [6] C. Guo, Y. Zheng, J. Ran, F. Xie, M. Jaroniec, S.-Z. Qiao, *Angew. Chem. Int. Ed.* **2017**, *56*, 8539–8543; *Angew. Chem.* **2017**, *129*, 8659–8663.
- [7] H. Yu, K. N. Dinh, Y. Sun, H. Fan, Y. Wang, Y. Jing, S. Li, M. Srinivasan, Q. Yan, *Nanoscale* **2018**, *10*, 14877–14884.
- [8] K. N. Dinh, Y. Sun, Z. Pei, Z. Yuan, A. Suwardi, Q. Huang, X. Liao, Z. Wang, Y. Chen, Q. Yan, *Small* **2020**, *16*, 1905885.
- [9] W. Li, W. Fang, C. Wu, K. N. Dinh, H. Ren, L. Zhao, C. Liu, Q. Yan, *J. Mater. Chem. A* **2020**, *8*, 3658–3666.
- [10] C. Zhang, S. Y. Hwang, A. Trout, Z. Peng, *J. Am. Chem. Soc.* **2014**, *136*, 7805–7808.
- [11] J. Chen, C. Fan, X. Hu, C. Wang, Z. Huang, G. Fu, J.-M. Lee, Y. Tang, *Small* **2019**, *15*, 1901518.
- [12] Q. Lu, J. Yu, X. Zou, K. Liao, P. Tan, W. Zhou, M. Ni, Z. Shao, *Adv. Funct. Mater.* **2019**, *29*, 1904481.
- [13] S. S. Shinde, C. H. Lee, J.-Y. Jung, N. K. Wagh, S.-H. Kim, D.-H. Kim, C. Lin, S. U. Lee, J.-H. Lee, *Energy Environ. Sci.* **2019**, *12*, 727–738.
- [14] Z. Cai, I. Yamada, S. Yagi, *ACS Appl. Mater. Interfaces* **2020**, *12*, 5847–5856.
- [15] C. Chen, D. Cheng, S. Liu, Z. Wang, M. Hu, K. Zhou, *Energy Storage Mater.* **2020**, *24*, 402–411.
- [16] M. S. Burke, L. J. Enman, A. S. Batchellor, S. Zou, S. W. Boettcher, *Chem. Mater.* **2015**, *27*, 7549–7558.
- [17] J. Pan, Y. Y. Xu, H. Yang, Z. Dong, H. Liu, B. Y. Xia, *Adv. Sci.* **2018**, *5*, 1700691.
- [18] G. Hai, X. Jia, K. Zhang, X. Liu, Z. Wu, G. Wang, *Nano Energy* **2018**, *44*, 345–352.
- [19] J. Wang, C. Cui, R. Lin, C. Xu, J. Wang, Z. Li, *Electrochim. Acta* **2018**, *286*, 397–405.
- [20] T. Wang, Z. Kou, S. Mu, J. Liu, D. He, I. S. Amiiniu, W. Meng, K. Zhou, Z. Luo, S. Chaemchuen, F. Verpoort, *Adv. Funct. Mater.* **2018**, *28*, 1705048.
- [21] B. Zhang, Z. Qi, Z. Wu, Y. H. Lui, T.-H. Kim, X. Tang, L. Zhou, W. Huang, S. Hu, *ACS Energy Lett.* **2018**, *4*, 328–336.
- [22] Y. Qian, T. An, E. Sarnello, Z. Liu, T. Li, D. Zhao, *ACS Appl. Energy Mater.* **2019**, *2*, 1784–1792.
- [23] B. Y. Guan, L. Yu, X. W. D. Lou, *Energy Environ. Sci.* **2016**, *9*, 3092–3096.
- [24] M. Zhang, Q. Dai, H. Zheng, M. Chen, L. Dai, *Adv. Mater.* **2018**, *30*, 1705431.
- [25] D. Ding, K. Shen, X. Chen, H. Chen, J. Chen, T. Fan, R. Wu, Y. Li, *ACS Catal.* **2018**, *8*, 7879–7888.
- [26] X. Zheng, Y. Cao, D. Liu, M. Cai, J. Ding, X. Liu, J. Wang, W. Hu, C. Zhong, *ACS Appl. Mater. Interfaces* **2019**, *11*, 15662–15669.
- [27] K. Rui, G. Zhao, Y. Chen, Y. Lin, Q. Zhou, J. Chen, J. Zhu, W. Sun, W. Huang, S. X. Dou, *Adv. Funct. Mater.* **2018**, *28*, 1801554.
- [28] F.-L. Li, Q. Shao, X. Huang, J.-P. Lang, *Angew. Chem. Int. Ed.* **2018**, *57*, 1888–1892; *Angew. Chem.* **2018**, *130*, 1906–1910.
- [29] L. Tao, C.-Y. Lin, S. Dou, S. Feng, D. Chen, D. Liu, J. Huo, Z. Xia, S. Wang, *Nano Energy* **2017**, *41*, 417–425.
- [30] J. Duan, S. Chen, C. Zhao, *Nat. Commun.* **2017**, *8*, 1–7.
- [31] L. Zhao, B. Dong, S. Li, L. Zhou, L. Lai, Z. Wang, S. Zhao, M. Han, K. Gao, M. Lu, X. Xie, B. Chen, Z. Liu, X. Wang, H. Zhang, H. Li, J. Liu, H. Zhang, X. Huang, W. Huang, *ACS Nano* **2017**, *11*, 5800–5807.
- [32] A. Mesbah, P. Rabu, R. Sibille, S. Lebègue, T. Mazet, B. Malaman, M. François, *Inorg. Chem.* **2014**, *53*, 872–881.
- [33] Z. Fang, B. Bueken, D. E. De Vos, R. A. Fischer, *Angew. Chem. Int. Ed.* **2015**, *54*, 7234–7254; *Angew. Chem.* **2015**, *127*, 7340–7362.
- [34] D. S. Raja, H.-W. Lin, S.-Y. Lu, *Nano Energy* **2019**, *57*, 1–13.
- [35] X. Zhao, B. Pattengale, D. Fan, Z. Zou, Y. Zhao, J. Du, J. Huang, C. Xu, *ACS Energy Lett.* **2018**, *3*, 2520–2526.
- [36] B. Wang, J. Shang, C. Guo, J. Zhang, F. Zhu, A. Han, J. Liu, *Small* **2019**, *15*, 1804761.
- [37] A. Dhakshinamoorthy, A. M. Asiri, H. Garcia, *Adv. Mater.* **2019**, *31*, 1900617.
- [38] M. Zhao, Y. Huang, Y. Peng, Z. Huang, Q. Ma, H. Zhang, *Chem. Soc. Rev.* **2018**, *47*, 6267–6295.
- [39] C. Hegde, X. Sun, K. N. Dinh, A. Huang, H. Ren, B. Li, R. Dangol, C. Liu, Z. Wang, Q. Yan, H. Li, *ACS Appl. Mater. Interfaces* **2020**, *12*, 2380–2389.
- [40] Z. Wu, Z. Zou, J. Huang, F. Gao, *J. Catal.* **2018**, *358*, 243–252.
- [41] M. Görlin, P. Chernev, J. Ferreira de Araújo, T. Reier, S. Dresp, B. Paul, R. Krähnert, H. Dau, P. Strasser, *J. Am. Chem. Soc.* **2016**, *138*, 5603–5614.
- [42] Y. Yang, H. Fei, G. Ruan, C. Xiang, J. M. Tour, *ACS Nano* **2014**, *8*, 9518–9523.
- [43] Z. Xue, Y. Li, Y. Zhang, W. Geng, B. Jia, J. Tang, S. Bao, H.-P. Wang, Y. Fan, Z.-w. Wei, Z. Zhang, Z. Ke, G. Li, C.-Y. Su, *Adv. Energy Mater.* **2018**, *8*, 1801564.
- [44] J. Yang, H. Liu, W. N. Martens, R. L. Frost, *J. Phys. Chem. C* **2010**, *114*, 111–119.
- [45] D. De Faria, S. Venâncio Silva, M. De Oliveira, *J. Raman Spectrosc.* **1997**, *28*, 873–878.
- [46] M. S. Burke, M. G. Kast, L. Trotochaud, A. M. Smith, S. W. Boettcher, *J. Am. Chem. Soc.* **2015**, *137*, 3638–3648.
- [47] C. Wei, Z. J. Xu, *Small Methods* **2018**, *2*, 1800168.
- [48] X. Han, X. Ling, Y. Wang, T. Ma, C. Zhong, W. Hu, Y. Deng, *Angew. Chem.* **2019**, *131*, 5413–5418.

Manuscript received: July 8, 2020

Revised manuscript received: August 1, 2020

Accepted manuscript online: August 2, 2020

Version of record online: August 24, 2020